



# Natural convection in a cubical cavity filled with a fluid showing temperature-dependent viscosity



Paola A. Córdoba <sup>a, c, \*</sup>, Nicolás Silin <sup>b, c</sup>, Enzo A. Dari <sup>a, c</sup>

<sup>a</sup> Departamento de Mecánica Computacional, Centro Atómico Bariloche-CNEA, Instituto Balseiro-UNCUYO, Av. Bustillo 9500, S.C. de Bariloche, Río Negro, Argentina

<sup>b</sup> Grupo de Materiales Nucleares, Centro Atómico Bariloche-CNEA, Instituto Balseiro-UNCUYO, Av. Bustillo 9500, S.C. de Bariloche, Río Negro, Argentina

<sup>c</sup> CONICET, Centro Atómico Bariloche-CNEA, Instituto Balseiro-UNCUYO, Av. Bustillo 9500, S.C. de Bariloche, Río Negro, Argentina

## ARTICLE INFO

### Article history:

Received 1 October 2014

Received in revised form

29 June 2015

Accepted 1 July 2015

Available online xxx

### Keywords:

Natural convection

Cubical cavity

Temperature-dependent viscosity

Finite element method

## ABSTRACT

We present a numerical and experimental study of laminar natural convection flow in a fluid filled cubical cavity. The fluid is a dielectric oil used for cooling distribution and power transformers. As most liquids, this oil exhibits temperature-dependent viscosity. The cubical cavity of interest has an imposed temperature difference between two opposite vertical walls while the other walls are insulated. The cavity dimensions are  $0.1 \text{ m} \times 0.1 \text{ m} \times 0.1 \text{ m}$ . Four characteristic Rayleigh numbers ranging from  $1.7 \times 10^8$  to  $6.3 \times 10^8$  were analyzed. The numerical study was carried out by applying the Finite Element Method to solve the 3D Navier–Stokes and heat equations using the in-house developed Par-GPFEP code. The influence of temperature-dependent viscosity on the total transferred heat and on the flow pattern, have been evaluated. Although there are several studies regarding the flow in a square cavity in this configuration, there is limited information in the literature on the 3D flow in cubical cavities with variable properties of the working fluid. We could not find in the open literature experimental measurements that we could use to validate our numerical results. For this reason an experimental setup was developed. The velocity field was visualized and measured by Particle Image Velocimetry (PIV). The temperature profiles in the vertical mid-axis at mid-plane of the cavity were measured and compared with the numerical results. We found reasonable agreement between numerical simulations and experimental measurements.

© 2015 Elsevier Masson SAS. All rights reserved.

## 1. Introduction

The problem of natural convection in a cubical cavity is a benchmark frequently used to validate CFD codes not only for its geometrical simplicity but also for its engineering interest. Thermal engineering applications range from double glazed windows, solar collectors, cooling of thermal-hydraulic devices, among others [1,2]. The simplest case is the cubical (square in the 2D approach) cavity with two opposite side walls differentially heated and the remaining four walls being adiabatic (from now on we will call this configuration CC).

Several studies regarding square cavities showing two dimensional behavior can be found in the literature, these cover a wide range of Rayleigh ( $Ra$ ) numbers ranging from  $10^3$  to  $10^{16}$ . The first report of a benchmark for this configuration is probably the work of De Vahl Davis [3], who presented flow results at steady state in a square cavity at a Prandtl ( $Pr$ ) number  $Pr = 0.71$  and Rayleigh numbers from  $10^3$  to  $10^6$ . A large number of authors have extended this range using different experimental and numerical techniques (e.g. Hyun and Lee [4]). Much of the work related to the square cavity has been reviewed by Arpino et al. [5] who also proposed a new square cavity benchmark solution at  $Ra = 10^7$  to  $10^8$ , his results were validated with numerical and experimental results from other authors (e.g. Le Quere [6]).

In contrast, the 3D problem of the flow in a cubical cavity has been less studied. On one hand the computational cost becomes higher, particularly with increasing Rayleigh numbers, and on the other, there are considerably fewer experimental studies to validate the numerical results. One of the first experimental studies was

\* Corresponding author. Departamento de Mecánica Computacional, Centro Atómico Bariloche-CNEA, Instituto Balseiro-UNCUYO, Av. Bustillo 9500, S.C. de Bariloche, Río Negro, Argentina.

E-mail address: [paolaco@cab.cnea.gov.ar](mailto:paolaco@cab.cnea.gov.ar) (P.A. Córdoba).

URL: <http://mecom.cnea.gov.ar/index.php/en>

presented by Hiller et al. [7] on a cubical cavity that was filled with a glycerol–water solution, covering a Rayleigh number range from  $10^4$  to  $10^7$ . They observed the temperature fields and flow streamlines, and found discrepancies with numerical results from other authors. The authors attribute these differences to the fact that the numerical model did not consider temperature dependent viscosity. More recently, Leong et al. and Mamun et al. [8–10] studied the cubical cavity in a different configuration: a cubical cavity with two opposing walls kept at different temperatures, the remaining walls with a lineal variation from the cold temperature to the hot temperature. They also studied the effect of the tilt angle of the cavity respect to the gravity force. They remark the fact that the other configurations like the CC benchmark are not physically-realizable. The reasoning behind this affirmation is that in an air-filled cavity the heat losses at the walls are especially critical due to the low thermal conductivity of the air.

With regard to numerical studies, the earliest work, to our knowledge, was that of Mallinson and Davis [11]. They studied the three-dimensional flow in a box, varying the cavity dimensions, the Rayleigh and  $Pr$  numbers. They analyzed how the three-dimensionality of the flow is affected by these three parameters. Most of the numerical studies focus on the air-filled cubical cavity, considering constant properties and Rayleigh numbers ranging from  $10^3$  to  $10^7$ . Some examples are the works of Refs. [12–16]. They used this benchmark (CC) to validate different numerical techniques. Pepper and Hollands [17] made a summary of several numerical studies of three benchmark problems, one of them is the air-filled enclosure proposed by Leong et al. [9], in a range of Rayleigh numbers from  $10^5$  to  $10^8$ . This configuration is convenient from both the experimental and numerical point of view not only for its experimental feasibility but also because it becomes unstable at lower  $Ra$  numbers. This allows to obtain unstable numerical solutions without the need of high spatial resolution [18].

On the other hand, some authors studied the effects of variable properties on laminar natural convection in an enclosure (e.g. Younis et al. [19]). Yamasaki and Irvine [20], studied the effects of temperature-dependent viscosity in a vertical tube. They found that the average velocity and the total heat transferred, increase when the variable viscosity is considered. Hyun and Lee [21] made a numerical study in a square cavity differentially heated with a fluid having a temperature-dependent viscosity at a Rayleigh number of  $3.5 \times 10^4$  and  $3.5 \times 10^5$ . They found that the variable viscosity affect the flow pattern and enhance the heat transfer in the cavity. Emery and Lee [22] studied the effects of temperature-dependent conductivity and viscosity for Prandtl numbers ranging from 0.01 to 1.0 and  $Ra \leq 10^6$ . In their work the viscosity and conductivity increase with temperature. They found that the temperature and velocity fields are affected by variable properties while the overall heat transfer remains unaffected.

In this work we present a numerical and experimental study of natural convection in the CC benchmark problem. The fluid is a dielectric oil used for cooling electrical equipment, specifically the YPF64 oil which is frequently used in distribution transformers using ONAN (oil-natural, air-natural) heat transfer management scheme. This mineral oil type has a strong viscosity variation in the working range of temperatures. The main objective is the observation and quantification of variable viscosity effects in the flow pattern and in the heat transfer rate in CC configuration. We studied four cases varying the Rayleigh number from  $1.7 \times 10^8$  to  $6.3 \times 10^8$  by changing the hot and cold wall temperatures. No turbulent model was used since the transition to turbulence begins between  $10^8$  to  $10^9$  [23,24] while our results (both numerical and experimental) do not suggest the development of turbulence.

## 2. Mathematical model

### 2.1. Geometry and general aspects

We consider a cubical enclosure with height, width and depth  $L$  as is illustrated in Fig. 1. The left and right vertical walls are both isothermal with temperature  $T_c$  and  $T_h$  ( $T_h > T_c$ ) respectively. The remaining four walls are thermally insulated. A mineral oil with temperature-dependent viscosity is the working fluid. The physical properties of the fluid are detailed in Section 2.4.

### 2.2. Governing equations

The cubical cavity flow is governed by the incompressible Navier–Stokes, and Energy equations, where the Boussinesq approximation is considered. The dimensional form of these equations can be expressed as

$$\rho_0[\partial_t u + (u \cdot \nabla)u] - \nabla \cdot [2\mu(T)\nabla^s u] + \nabla p = f \quad \text{in } \Omega, t \in (0, T), \quad (1)$$

$$\nabla \cdot u = 0 \quad \text{in } \Omega, t \in (0, T), \quad (2)$$

$$\rho_0 C_p [\partial_t T + (u \cdot \nabla)T] - k \nabla^2 T = 0 \quad \text{in } \Omega, t \in (0, T), \quad (3)$$

where  $u$  is the velocity vector with components  $u_x$ ,  $u_y$  and  $u_z$ . The buoyancy force is  $f = \rho_0 g [1 - \beta(T - T_0)]$ , being  $\rho_0$  the density at the temperature  $T_0$ . The buoyancy force is written in this form to avoid the density evaluation at the local temperature.  $\nabla^s u = \frac{1}{2}[(\nabla u) + (\nabla u)^T]$  is the symmetric gradient operator.  $\Omega$  is the  $N$ -dimensional domain where the problem will be solved in the time interval  $(0, T)$ . We use the no-slip boundary conditions for velocity at all walls,

$$u_x = u_y = u_z = 0 \quad \text{at} \quad \begin{cases} x = 0, & L, \\ y = 0, & L, \\ z = 0, & L. \end{cases} \quad (4)$$

For the energy equation, the left and right vertical walls have Dirichlet boundary conditions (5) with  $T_h$  and  $T_c$  constant values while the other four walls have Neumann conditions (6).

$$\begin{aligned} T(L, y, z) &= T_h \quad \text{at } x = L, \\ T(0, y, z) &= T_c \quad \text{at } x = 0, \end{aligned} \quad (5)$$

$$\begin{aligned} \frac{\partial T}{\partial y} &= 0 \quad \text{at } y = 0, L, \\ \frac{\partial T}{\partial z} &= 0 \quad \text{at } z = 0, L. \end{aligned} \quad (6)$$

We are interested in the steady state solution of this problem, however the code is also able to solve the transitory to observe the flow structures of the transient state. The time necessary to reach

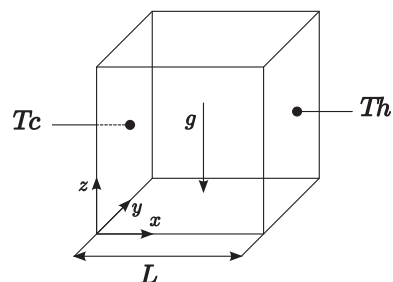


Fig. 1. Geometrical description of the cavity and coordinates system.

the steady state is approximately one hour starting from constant initial conditions. Such conditions were: null velocity in the whole domain and ambient temperature (20°C) in all domain except in the isothermal walls.

### 2.3. Solution method

The equations (1)–(3) have been solved by the Finite Element Method. In this work we use the Standard Galerkin approximation with the addition of stabilizer terms according to the SUPG method [25]. With this technique, the variational formulation of problem (1)–(3) consists in finding finite element approximations  $(u_h^{n+\theta}, p_h^{n+1}, T_h^{n+\theta})$  to  $(u^{n+\theta}, p^{n+1}, T^{n+\theta})$  such that

$$\begin{aligned} & \rho_0 \left( \frac{u_h^{n+1} - u_h^n}{\Delta t} + (u_h^n \cdot \nabla) u_h^{n+\theta}, v_h \right) + 2\mu(T_h^n) \cdot a(u_h^{n+\theta}, v_h) \\ & - b(p_h^{n+1}, v_h) - (f^n, v_h) + \sum_{e=1}^{nel} \int_{\Omega^e} (\mathcal{P}(u_h, v_h) \tau \mathcal{R}(u_h, p_h) \\ & + (4\mu + 2\rho_0 \|u_h^n\| h_e) \nabla \cdot u_h^{n+1} \nabla \cdot v_h) d\Omega = 0 \quad \forall v_h \in V_{h,0}, \end{aligned} \quad (7)$$

$$b(q_h, u_h^{n+1}) + \sum_{e=1}^{nel} \int_{\Omega^e} \tau \mathcal{R}(u_h, p_h) \cdot \nabla q_h d\Omega = 0 \quad \forall q_h \in Q_h, \quad (8)$$

$$\begin{aligned} & \left( \frac{T_h^{n+1} - T_h^n}{\Delta t} + (u_h^n \cdot \nabla) T_h^{n+\theta}, w_h \right) + \alpha \cdot a(T_h^{n+\theta}, w_h) \\ & + \sum_{e=1}^{nel} \int_{\Omega^e} \mathcal{P}(u_h, w_h) \tau_1 (u_h^n \cdot \nabla) T_h^{n+\theta} d\Omega = 0 \quad \forall w_h \in W_h, \end{aligned} \quad (9)$$

with the finite element spaces  $Q_h, V_h, V_{h,0}$  and  $W_h$  which are approximations to  $Q_{st} = \{q \in L^2(\Omega) \mid \int_{\Omega} q = 0\}$ ,  $H^1(\Omega)^N$ ,  $V_{st} = H_0^1(\Omega)^N$  and  $W_{st} = H_D^1(\Omega)^N$  respectively with the following bilinear forms:

$$\begin{aligned} a(u_h^{n+\theta}, v_h) &:= (\nabla^s u_h^{n+\theta}, \nabla^s v_h), \\ b(q_h, u_h^{n+1}) &:= (q_h, \nabla \cdot u_h^{n+1}), \end{aligned} \quad (10)$$

the perturbation to the test function  $\mathcal{P}$  of the form:

$$\mathcal{P}(u_h, v_h) = (u_h \cdot \nabla) v_h, \quad (11)$$

and  $\mathcal{R}$  the residual of the momentum equation

$$\mathcal{R}(u_h, p_h) = \rho_0 \left[ \frac{u_h^{n+1} - u_h^n}{\Delta t} + (u_h^n \cdot \nabla) u_h^{n+\theta} \right] + \nabla p_h^{n+1} - f^n, \quad (12)$$

$\tau$  is the intrinsic time that depends of the stabilizing technique, we use the definition of Codina [25] for momentum and energy equations respectively, written as follows,

$$\tau = \frac{1}{\frac{4\mu}{\rho_0 h_e^2} + \frac{2\|u\|}{h_e}} \quad \tau_1 = \frac{1}{\frac{4\alpha}{h_e^2} + \frac{2\|u\|}{h_e}}, \quad (13)$$

where  $h_e$  is the element size in the flow direction. For the temporal discretization we use the trapezoidal rule scheme:

$$u^{n+\theta} := \theta u^{n+1} + (1 - \theta) u^n. \quad (14)$$

In this work we use  $\theta = 1/2$  (Crank–Nicolson) for the

momentum equation and  $\theta = 1$  (Backward Euler) for the energy equation. A detailed discussion about this scheme can be found in [26]. The resulting system of linear equations was solved by the iterative method GMRES with a block-ILU preconditioner using PETSc and MPI as parallelization method, which is implemented in the in-house developed Par-GPFE code [27].

### 2.4. Temperature viscosity dependence

The working fluid is a mineral naphthenic YPF64 oil. The physical properties of this mineral oil were provided by Tubos Trans Electric S.A. and they are detailed in Table 1.

One of the characteristics of this oil is the viscosity dependence on temperature. Due to the limited technical specifications, related with the hydrodynamic properties, available for this mineral oil, we measured the viscosity of the oil for the working temperature range by means of a Brookfield DV-II + Pro programmable cone/plate viscometer. To provide a controlled variation of temperature, a HAAKE D8 temperature bath controller coupled to the viscometer was used. The viscosity measurements are shown in Fig. 2.

Fig. 2 shows the experimental data and its fitting function in logarithmic scale. We found that the viscosity of the working oil can be fitted with the following law:

$$\log(\mu(T)) = B - A \log(T), \quad (15)$$

where  $A = 9.55 \pm 0.23$ ,  $B = 50.24 \pm 1.33$ , for  $\mu$  is expressed in kg/ms and temperature  $T$  in Kelvin.

This exponential law was implemented in the solver code to account for viscosity variations with temperature.

Since the kinematic viscosity is the parameter with strongest temperature dependence as compared to the thermal conductivity and the specific heat in the working temperature range [28], in the present work, all the thermal oil properties were considered constants except the viscosity.

The wall temperatures and the respective Rayleigh and Prandtl numbers for each case studied are presented in Table 2. The Rayleigh and Prandtl number were calculated according the equations (16) and (17). The fluid properties are evaluated using a reference temperature  $T_f = (T_h + T_c)/2$ .

$$Ra_L = \frac{g\beta(T_h - T_c)L^3}{\nu\alpha}, \quad (16)$$

$$Pr = \frac{\nu}{\alpha}, \quad (17)$$

Notice that for the wall temperatures in case 1, the dynamic viscosity varies from ~0.007 to ~0.013 kg/ms, resulting in a variation with respect to the mean value ( $\Delta\mu/\bar{\mu}$ ), of ~60%, this viscosity variation increases with  $T_h - T_c$  temperature difference, reaching about ~103% for case 4.

### 2.5. Characteristic scales and grid size

In order to determine the grid size, a first estimation of the thickness of the thermal and momentum boundary layers ( $\delta_\theta, \delta$ )

**Table 1**  
Fluid properties of the YPF64 oil.

Physical property		Value
Density (kg/m <sup>3</sup> )	$\rho$	880
Thermal conductivity (W/m K)	$k$	0.126
Specific Heat (J/kg K)	$C_p$	1860
Thermal diffusivity (m <sup>2</sup> /s)	$\alpha$	$7.7 \times 10^{-8}$
Thermal expansion coefficient (K <sup>-1</sup> )	$\beta$	0.00075

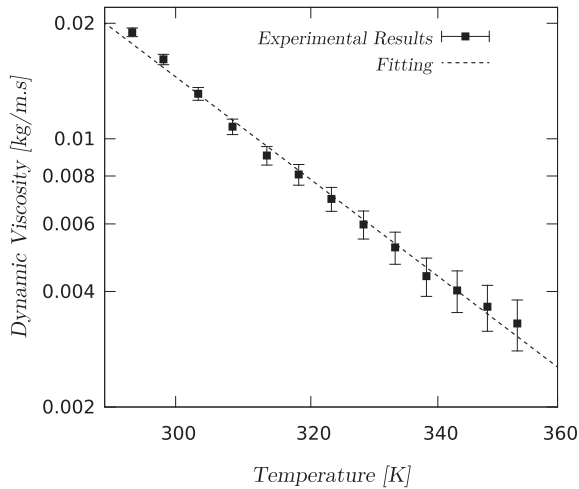


**Fig. 2.** Characteristic curve of the viscosity as a function of temperature for mineral oil YPF64 in logarithmic scale.

**Table 2**  
Characteristic quantities in the four cases studied.

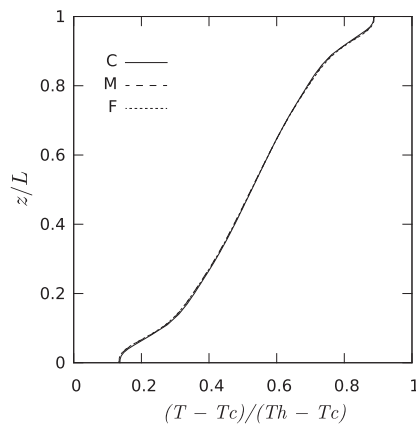
	$T_h$	$T_c$	$Pr$	$Ra$	$\Delta\mu/\bar{\mu}$
Case 1	50	30	142.02	$1.7 \times 10^8$	60%
Case 2	60	30	122.08	$3.0 \times 10^8$	85%
Case 3	70	35	97.72	$4.4 \times 10^8$	95%
Case 4	80	40	78.62	$6.3 \times 10^8$	103%

**Table 3**  
Grid dependence of Nusselt number in different meshes.

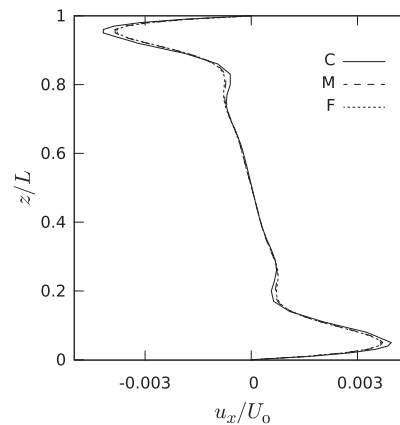
Mesh	Grid size	$\bar{Nu}$ (hot wall)	$\bar{Nu}$ (cold wall)	$h_{min}$ (m)
C	$50 \times 50 \times 50$	35.04	35.13	$5.00 \times 10^{-4}$
M	$120 \times 120 \times 120$	36.27	35.97	$2.50 \times 10^{-4}$
F	$150 \times 150 \times 150$	36.27	36.20	$1.42 \times 10^{-4}$

was made using the approximation (18) based on the Nusselt number  $Nu$  and the characteristic length  $l$  [29].

$$\delta_\theta \sim \frac{l}{Nu}, \quad (18)$$



(a)



(b)

**Fig. 3.** Vertical profiles at mid-plane of the cavity obtained from steady state numerical solutions using three different meshes: C, M and F (see Table 3). (a) Temperature profile at  $x = 0.5$ ,  $y = 0.5$  (Mid-plane), (b) x-component of velocity profile at  $x = 0.5$ ,  $y = 0.5$ .

$$Nu = 0.18 \left( \frac{Pr}{0.2 + Pr} Ra_L \right)^{0.29}, \quad (19)$$

with the assumption of  $\delta_\theta \sim \delta$ . The Nusselt number can be estimated by means of an empirical correlation for natural convection in enclosures (19) (see [30]). In our case, with a  $Ra = 1.7 \times 10^8$  and  $Pr = 142$ , the value of  $\delta_\theta$  is about  $2.3 \times 10^{-3}$  m. Taking into account the thickness of the boundary layer, three non-uniform grids were built and used in order to make a grid dependency study. Table 3 shows the minimal spatial discretization  $h_{min}$  and also, the dependence of total heat transfer with the grid size. It can be noted that the difference between the numerically calculated Nusselt numbers for cases C and M is about 3.4% whereas the difference between cases M and F is much lower, about 0.07%. This is also reflected in Fig. 3 which presents the vertical profiles of temperature and velocity at mid-plane of the cavity for the three mesh sizes at steady state. We used vertical profiles along vertical mid axis of the cavity mid plane since we obtained experimental data over this symmetry axis, not only for temperature but also for velocity as we described in Section 3. The velocity is presented in a dimensionless form by using the characteristic velocity  $U_0 = (g\beta L(T_h - T_c))^{1/2}$ . The results obtained for M and F are practically grid independent and also can resolve the boundary layers near the walls. For cases 3 and 4 with boundary layer thicknesses around  $1.7 \times 10^{-3}$  m and  $1.6 \times 10^{-3}$  m respectively, the mesh F was used to improve the spatial resolution near the walls.

### 3. Experimental setup and measurement method

The experimental device is a cubical cavity completely filled with mineral oil YPF64. The cavity is formed by two vertical and opposed aluminum walls and four transparent walls. The superior wall is made of 4 mm thick crystal acrylic and the remaining three are made of window glass. The spacing between walls is  $100 \pm 0.5$  mm. A schematic of the experimental device is shown in Fig. 4 (Top).

The upper wall has two 4 mm penetrations, one for the insertion of the traversing temperature sensor and the other for the expansion tank. This tank is used to compensate volume changes due to thermal expansion of the oil and the materials of the cavity. The aluminum walls provide the hot and cold constant temperature conditions. The hot wall is 24 mm thick and is heated by means of a Watlow FIREROD cartridge electrical heater, with diameter and

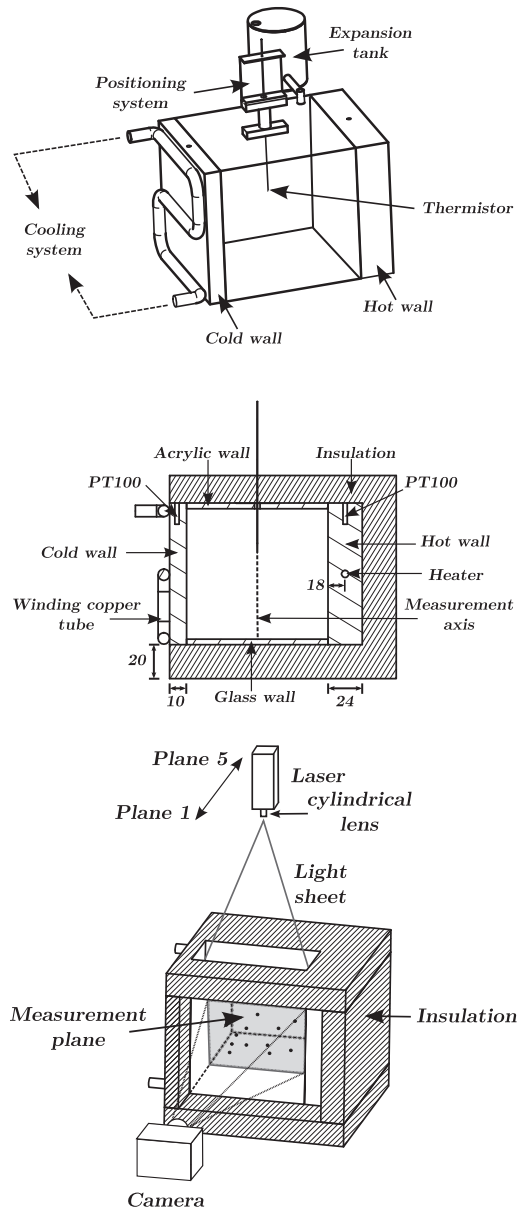


**Fig. 4.** Schematic of the experimental device. (Top) Cavity scheme, (Center) Cavity mid-section showing the insulation, (Bottom) PIV recording setup. Laser sheet is positioned at different distances from the viewing window, Plane 1 is closest while Plane 5 corresponds to mid-plane.

heating length of 6.5 mm and 50 mm respectively. The heater was inserted parallel to the internal face of the hot wall, at a distance of 18 mm. The temperature is controlled by a Novus N480D temperature controller in PID mode. The power is determined by measuring the instantaneous applied tension and taking the square average. With this value and the heater resistance the applied total electrical power was calculated. The cold wall is refrigerated by means of a glycol and water mixture flow supplied by a thermostatic bath. The fluid is passed by a winding copper tube soldered to a flat slab that is in good thermal contact with the aluminum wall. Two PT100 transducers are inserted into the hot and cold walls to measure their temperature.

The measurement of the oil temperature is very challenging. We consider the most relevant information is given by the vertical temperature profile along the central vertical symmetry axis. To obtain this temperature profile a 0.5 mm diameter traversing glass

beard thermistor was used. The thermo probe was calibrated by means of a Tecne Tecal 650S temperature calibrator giving a measurement precision of 0.5°C. Temperature measurements were taken by a National Instruments NI 9219 universal analog input module. Heater voltage measurements were taken by means of a resistor divider bridge connected to a NI 9205 analog input module. Both were connected to a PC. The cavity was covered with 20 mm thick expanded polystyrene to provide the thermal insulation of the cavity (see Fig. 4 (Center)). The thermal conductivity of the expanded polystyrene is approximately  $k_{wall} = 0.04$  W/mK.

The vertical temperature profile was measured once the steady state was achieved, with the thermistor moving along the central vertical symmetry axis of the cavity. Steady state was based on the settling times obtained from simulations being approximately one hour. Measurements were taken using the insulation configuration as shown in the cavity cross section in Fig. 4 (Center), where the insulation wall covers all the cavity except the cold wall.

We used Particle Image Velocimetry (PIV) to obtain the experimental velocity fields. A detailed description of this technique can be found in [31–33]. This requires a different configuration as shown in Fig. 4 (Bottom), where the frontal wall (visualization window) and one half of the top wall (illumination window) were not covered by insulation. The first one was necessary for visualization and the second one to provide the illumination entry.

Fig. 4 (Bottom) also shows a sketch of the setup used for PIV recording in the cubical cavity. Due to the low velocities involved, approximately  $\sim 10^{-3}$  m/s, a digital camera able to capture images at a frame rate up to 5 frames per second (fps) and a laser in continuous mode, were appropriate to obtain satisfactory velocity measurements. We used a laser with a nominal power of 400 mW, a wave length of 532 nm and an aperture angle of 30°. The images were captured with a Casio EX-FH25 digital camera in burst mode. A cylindrical lens is used to expand the laser in order to generate a light sheet that illuminates the measurement plane.

This plane can be located at different offsets from the frontal window in direction to the cavity mid plane. Five planes were measured. Those are located at  $y = 0.01$  m (plane 1),  $y = 0.02$  m (plane 2),  $y = 0.03$  m (plane 3),  $y = 0.04$  m (plane 4) and  $y = 0.05$  m (plane 5), being  $y = 0$  the frontal window. With the dimensionless notation  $y^* = y/L$ , the planes are located at  $y^* = 0.1, 0.2, 0.3, 0.4$  and  $0.5$  respectively. The last one also corresponds to cavity mid-plane.

Spherical hollow glass particles 10  $\mu$ m in diameter were used as flow tracers. When these particles are illuminated the scattered light is recorded by the digital camera focusing perpendicular to the laser (see Fig. 4 (Bottom)).

## 4. Results and discussion

### 4.1. Numerical results

We performed numerical simulations for the four cases detailed in Table 2 in order to study the heat transfer and the flow pattern in a fluid with variable viscosity. The dependence of the viscosity with temperature is described by the potential law equation (15). The numerical results are later compared with the experimental measurements.

The flow pattern at different times of the initial transient, along with the temperature distribution at cavity mid-plane for case 1, are shown in Fig. 5. The flow pattern at steady state for cases 2, 3 and 4 are visualized in Fig. 6.

In Fig. 5 we show at left side the plane nearest to the window wall (plane 1), at center, the streamlines pattern at cavity mid-plane and at right side the temperature distribution at this plane. The streamlines are obtained as a result of the velocity field projection over the xy plane to provide a better visualization and a



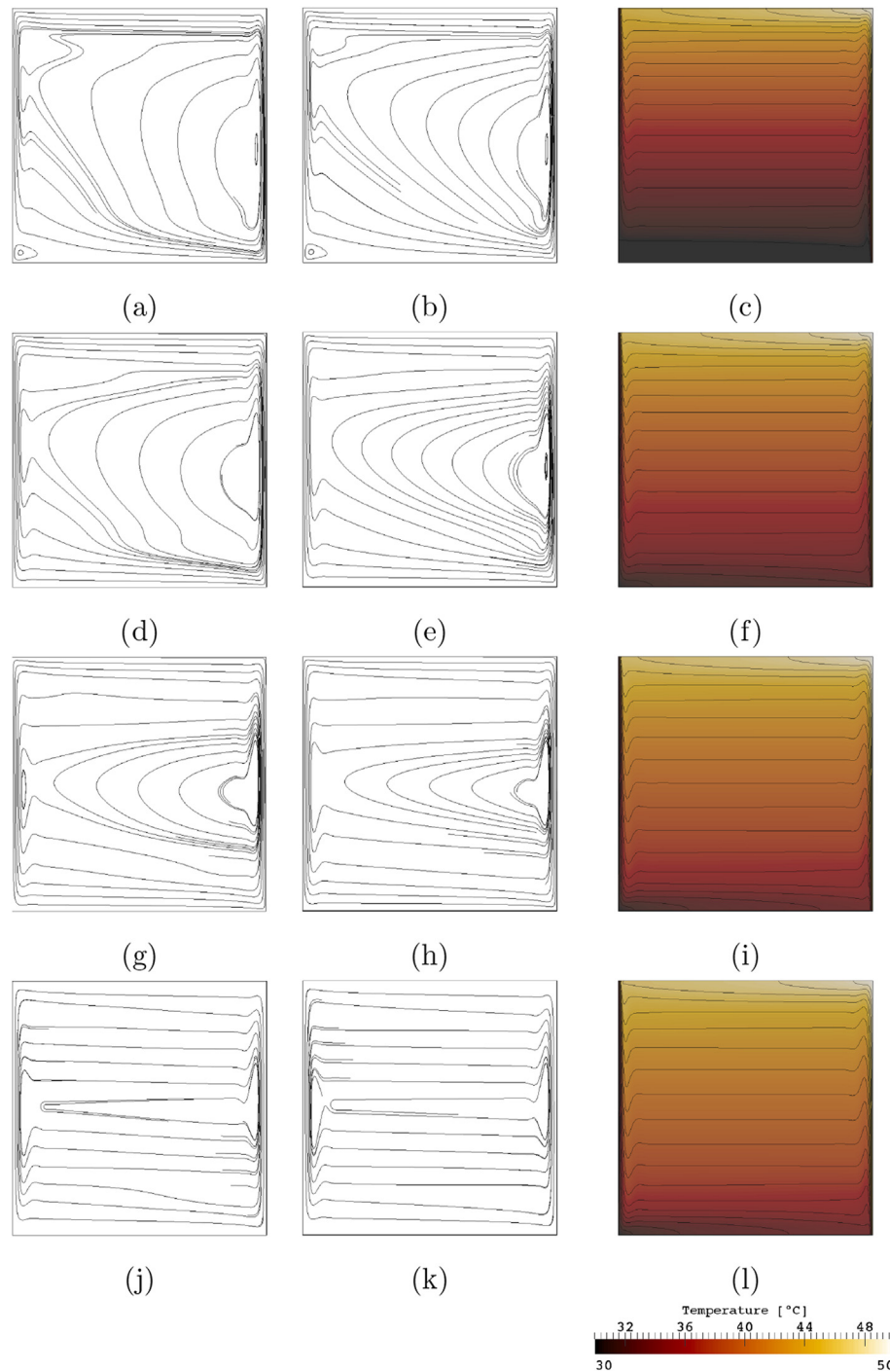


**Fig. 5.** Streamlines and Isotherms at different times of the unsteady state at  $Ra = 1.7 \times 10^8$  until reaching the steady state (Case 1 Numerical). Plane 1 (left), Mid-Plane (center) and temperature distribution and isotherms at mid plane (right). (a), (b), (c)  $t = 1250$  s, (d), (e), (f)  $t = 2000$  s, (g), (h), (i)  $t = 3250$  s, (j), (k), (l)  $t = 4500$  s (steady state solution).

direct comparison with the measured 2D velocity fields. At these Rayleigh numbers ( $Ra \sim 10^8$ ), the flow is essentially convective. The flow in counter clockwise direction is produced by the buoyancy force due to the temperature gradient between the isothermal walls. Due to the non uniform temperature, regions with lower and higher viscosity and consequently thinner and thicker boundary layers exist in the entire cavity.

Notice that at  $t = 1250$  s (see Fig. 5 (a)–(c)), two new rolls appear near the upper and lower left corners, which are later dissipated (see Fig. 5 (d)–(i)). As time increases, it can be seen that an

elongated central vortex core forms at mid-height of the cavity (see Fig. 5 (g)–(h)). Thus, when the convective process is developed, the flow pattern at these Rayleigh numbers is characterized by the presence of three vortices (see Fig. 5 (k)). Most of the flow rate inside the cavity is transported by the central vortex which corresponds to the main flow following the cavity geometry. The other two vortices, vertical and adjacent to the isothermal walls, constitute a second order phenomenon. With regard to the flow pattern, the main difference found between case 1 and cases 2 to 4 was the aspect of the central vortex core. In the case 1, this elongated

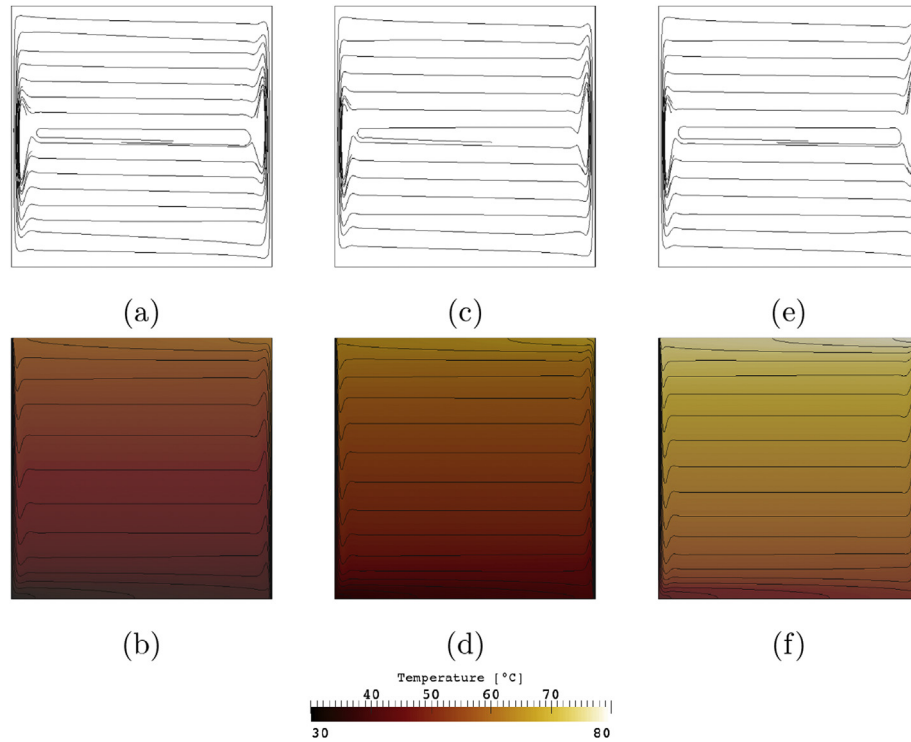


**Fig. 6.** Streamlines and Isotherms at vertical mid-plane (Steady state numerical solution). Streamlines (top), Temperature distribution and isotherms (bottom). (a), (b) case 2, (c), (d) case 3, (e), (f) case 4.

convective roll is asymmetric, being wider near the hot wall where the viscosity is smaller and narrower near the cold wall where the viscosity is maximal. This asymmetry decreases as the Rayleigh number increases, being almost negligible in case 4 (see Fig. 6).

The asymmetry caused by variations in the fluid viscosity has also been documented by Hyun and Lee [21]. They show streamlines of the flow at different times in the start transitory. They found that at  $Ra = 3.5 \times 10^5$ , the streamlines are more concentrated near the hot wall than near the cold one and the secondary roll near the hot wall was observed to be larger. In our case, despite the strong variations on viscosity in all cases, the asymmetry regarding the central vortex core is barely noticeable. A difference most likely caused by the higher  $Ra$  number.

In the present work, with Rayleigh numbers in the range of  $1.7\text{--}6.3 \times 10^8$ , the maximum velocities are present near the hot and

cold walls. An appreciable difference was found between the boundary layer thicknesses on the vertical and horizontal walls. This is expected as the fluid movement is generated by different mechanisms. This behavior is observed quantitatively in the vertical and horizontal velocity profiles along the cavity mid axis shown in Fig. 7 (a) and (b). We called horizontal profile to a sampling of velocity  $z$ -component along  $x$ -direction over horizontal mid axis of each plane and vertical profile to a sampling of velocity  $x$ -component along  $z$ -direction over vertical mid axis of each plane (see the insets in Fig. 7 (a) and (b)). In this figure we can be seen that in the central core region velocities are two orders of magnitude lower due to stratification. It can also be seen that, while the profiles of the vertical velocity component are not affected by boundary effects of the end walls (see Fig. 7(a)), the ones of the horizontal velocity (see Fig. 7(b)) clearly show the 3D nature of the flow.

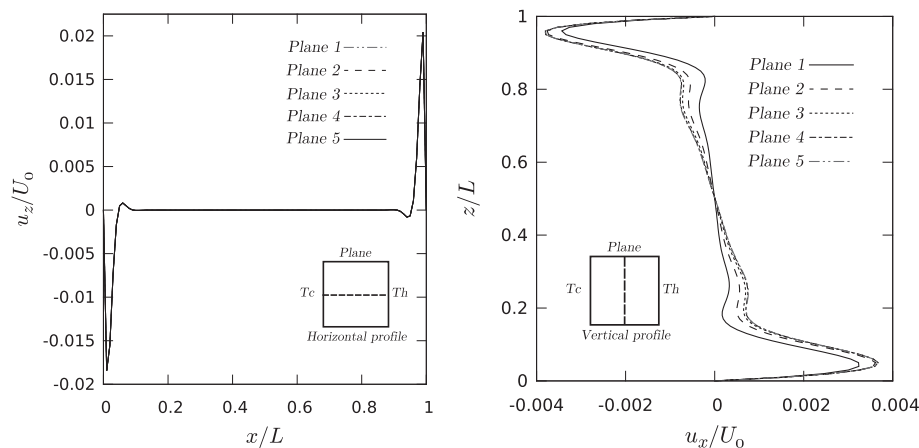


**Fig. 7.** (a) and (b) Velocity profiles at different planes of the cavity. (a) Vertical velocity profiles over the horizontal mid axis of each plane, (b) Horizontal velocity profiles over the vertical mid axis of each plane. The insets show the profile locations.

**Table 4**

Comparison of Nusselt number and vertical and horizontal velocity profile peak values and locations for numerical and experimental results.

			$\overline{Nu}$	$u_x/U_0 (x = 0.5)$	$z/L(x = 0.5)$	$u_z/U_0(z = 0.5)$	$x/L(z = 0.5)$
Case 1	Num.	(hw)	36.27	−0.00380	0.955	0.0204	0.99
		(cw)	36.20	0.00367	0.050	−0.0184	0.01
	Exp.		45 ± 6	−0.00461	0.960	0.0198	1.0
Case 2	Num.	(hw)	41.51	−0.00388	0.960	0.0223	0.99
		(cw)	41.44	0.00360	0.045	−0.0201	0.01
	Exp.		56 ± 5	−0.00501	0.970	0.0161	1.0
Case 3	Num.	(hw)	45.69	−0.00409	0.960	0.0244	0.99
		(cw)	45.55	0.00380	0.040	−0.0226	0.01
	Exp.		59 ± 6	−0.00498	0.970	0.0164	1.0
Case 4	Num.	(hw)	49.88	0.00332	0.050	−0.00896	0.01
		(cw)	49.78	−0.00434	0.970	0.0262	0.99
	Exp.		68 ± 6	0.00400	0.040	−0.0251	0.01
				−0.00546	0.980	0.00997	1.0
				0.00372	0.040	−0.00460	0.01

Regarding temperature fields, Figs. 5 (l), 6 (b), (d) and (f) show cavity mid-plane temperature distribution and isotherms, notice that isotherms are irregular only near the walls due to the boundary layers. Most of the cavity shows a vertical stratification, with negligible horizontal temperature gradients except near the hot and cold walls. On the other hand vertical temperature gradients are almost constant in the central area.

#### 4.2. Experimental results

In this section we show a comparison between the Nusselt number and temperature profiles obtained from simulations and

experiment. We also compare the flow patterns from the experimental measurements and numerical simulations. The Nusselt number is a dimensionless number defined as follows [30],

$$Nu_L = \frac{hL}{k_f} = \frac{\dot{q}L}{Ak_f(T_h - T_c)} \quad (20)$$

where  $h$  is the convective heat transfer coefficient,  $L$  is the geometrical characteristic length,  $k_f$  is the fluid thermal conductivity,  $\dot{q}$  is the total heat transferred to the system and  $A$  is the surface area. Numerically, the mean Nusselt is calculated by the expression (21). Experimentally, this dimensionless number is

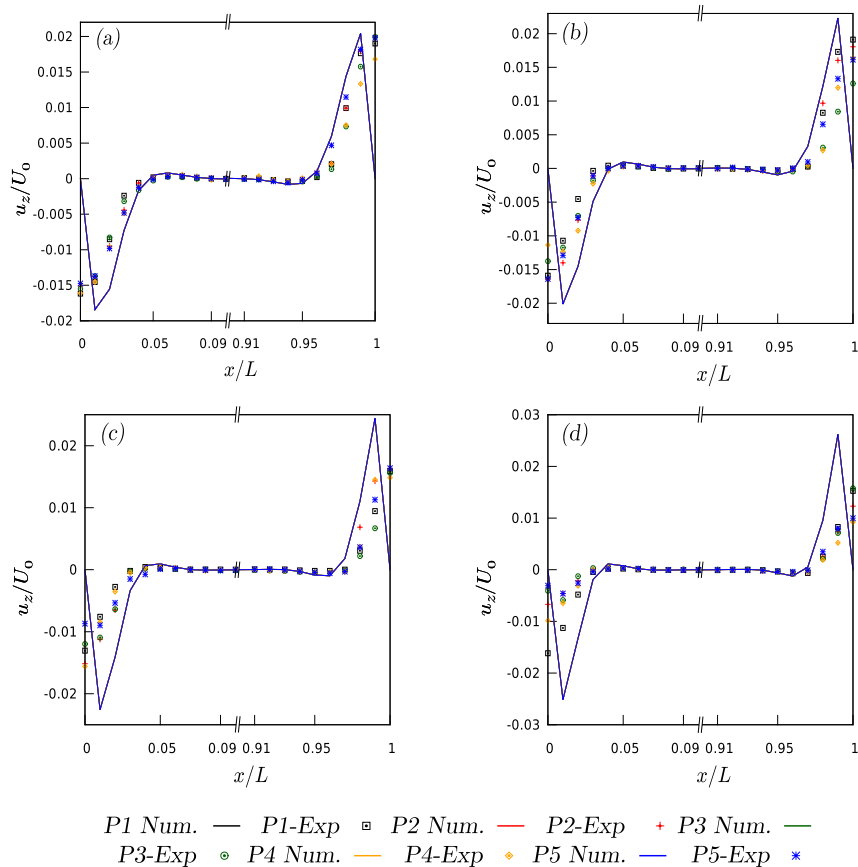


**Fig. 8.** Numerical and experimental horizontal velocity profiles at different heights of the cavity in the four cases. (a) Case 1, (b) Case 2, (c) Case 3, (d) Case 4.



calculated by the expression (20) using the measured power  $\dot{q}_{avg} = (V_{rms})^2/R - \dot{q}_{Losses}$ , where  $V_{rms}$  is the heater voltage input and  $R$  is the heater resistance and  $\dot{q}_{Losses}$  are the power losses. These power losses were roughly estimated based on the thermal resistivity of the isolation material and subtracted from the total applied electrical power to calculate the heat flux to the working fluid. These measured and calculated Nusselt values, along with the

vertical and horizontal velocity profile peak values, are summarized in Table 4.

$$\overline{Nu}_L = \frac{L}{T_h - T_c} \left( \frac{1}{A} \int_{Wall} \frac{\partial T}{\partial x} d\Gamma \right) \quad (21)$$

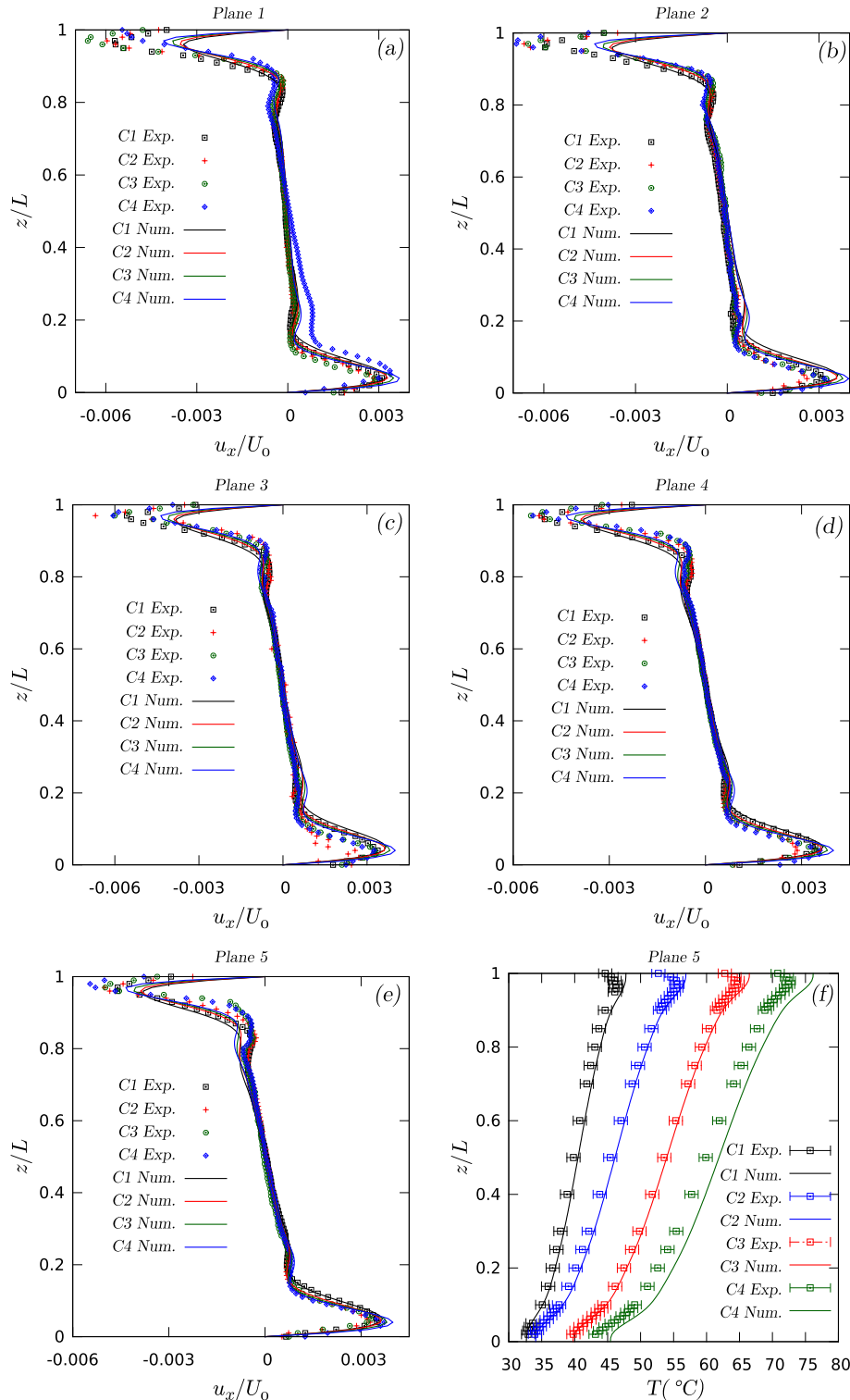


**Fig. 9.** (a)–(e) Numerical and experimental vertical velocity profiles at  $x = 0.5$ , among different cases by planes. (f) Comparison of vertical temperature profiles at mid-plane of the cavity between experimental and numerical results in the four cases.

As can be seen in Table 4, there is a difference between the calculated Nusselt number and the one obtained from experimental measurement, the maximum difference is approximately 27% with respect to the measured value for case 4 and the minimum is around 20% for case 1. This discrepancy may be caused by the uncertainty associated to the heat losses in the insulation system that can not be predicted by the simplified mathematical model. However in our case, the estimated heat losses correspond only to approximately 13% of the measured total power. Even then this difference can not be justified completely by measurement uncertainty.

In Figs. 8 and 9 (a)–(e) we show the horizontal and vertical velocity profiles from different cavity planes for all the studied cases. Fig. 8 shows the horizontal velocity profiles along the cavity mid axis  $z/L = 0.5$ , at five different measurement planes (P1, P2... P5), located at  $y/L = 0.1, 0.2... 0.5$  respectively, for each case studied. Notice that reasonable agreement exist between experimental and numerical results for case 1. However it can be observed that in all cases the minimum and maximum experimental velocity values are registered at  $x/L = 0$  and  $x/L = 1$  respectively showing an insufficient resolution near the walls. As Rayleigh number increases the boundary layers become thinner and the experimental results obtained for cases 2, 3 and 4 can be only interpreted as spatially averaged velocity values near the isothermal walls. It is clear that a higher experimental resolution is required to measure the boundary layers near the isothermal walls where the boundary layers become thinner. In the present study we were interested in capturing the entire velocity field, however a higher resolution near the isothermal walls would require to focus in the region of interest.

In Fig. 9 (a)–(e) for each plane, vertical velocity profiles of the four cases studied are plotted. Notice that in these cases a satisfactory resolution could be obtained, resolving the lower velocities near the top and bottom walls. A reasonable agreement can be observed between calculated and measured velocities along the 90% of the  $z$  mid-axis. The greatest discrepancies are registered near the top wall. On this upper region the measured velocities are higher than the values obtained from numerical simulation.

On the other hand, in spite of the difference between the numerical and experimental Nusselt values observed in Table 4, we can see in Fig. 9 (f) a reasonable agreement between the measurements and the numerical solution. This figure shows the temperature profiles along the central  $z$ -axis located at mid-plane

of the cavity. The difference observed in the temperature profile upper region is most likely caused by the opening used to introduce the temperature sensor.

The measured flow pattern in case 4 is shown in Fig. 10. There are clear differences with the numerical fully developed solution. Most notoriously the asymmetry of the central convective vortex. On the other hand the experimental results compare well with the numerical transient solution, showing qualitatively similar characteristics. One of them is the convective roll near the upper left corner which is present in all planes measured, as well as the presence of the three vortices: the main flow with a central and asymmetric core and the two vortices near the isothermal walls. Therefore, based on the flow pattern obtained experimentally, we can venture the flow in the experiment has not reached a fully steady state condition at the time of the measurement. This can also explain the main differences between numerical and experimental results. First, the velocities during the transient are higher than the steady state ones. Second, at higher velocities, higher Nusselt numbers are obtained and third, the flow pattern is significantly asymmetric during the initial transient. The experiment duration was defined from the simulation settling times, being approximately one hour. In the present study longer times were difficult to achieve due to limitations in the experimental device and therefore this remains as an open topic for future work.

## 5. Conclusions

The present numerical study provides the basic flow patterns and heat transfer characteristics for natural convection in a cubical cavity with variable viscosity at Rayleigh numbers from  $Ra = 1.7 \times 10^8$  to  $Ra = 6.3 \times 10^8$  with a reasonable agreement with the experimental data.

The experimental results suggest fully developed conditions were not achieved at the measurement time. This fact can explain the discrepancies between numerical and experimental results. Thus, higher Nusselt numbers and velocities were found in the measured results as compared to numerical ones. In spite of these differences, the size of the thermal and velocity boundary layers, as well as the velocity and temperature scales in both experimental and numerical cases are in good agreement.

The numerical and experimental flow patterns present a non-oscillatory behavior, reflecting a stable convective flow. This is not expected for the Rayleigh numbers studied, which correspond to conditions reported as unstable [23,24].

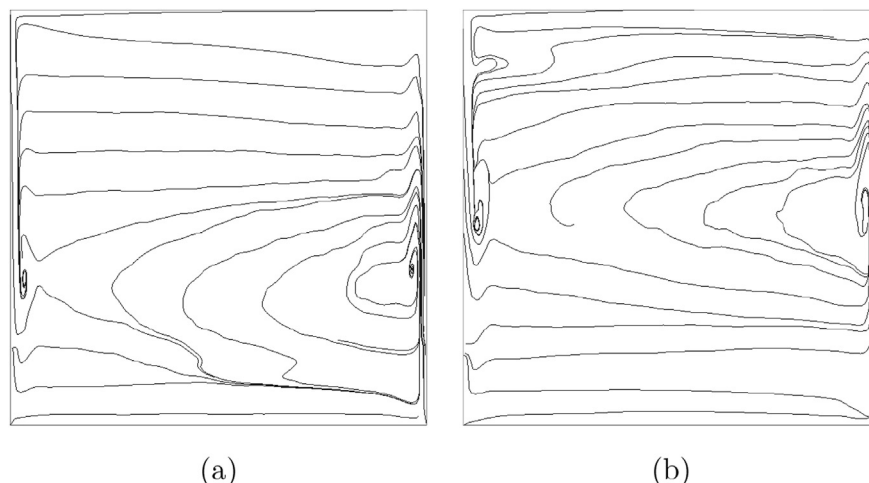


Fig. 10. Streamlines at different vertical planes of the cavity at  $Ra = 6.31 \times 10^8$  (Case 4 Experimental). (a)  $y/L = 0.1$ , (b)  $y/L = 0.5$ .

It would be interesting to include more realistic boundary conditions in the numerical model for further investigations and also improve the experimental setup to reduce the principal heat losses and stabilization times.

The temperature viscosity dependence causes a barely noticeable asymmetry in the flow velocity field at steady state. This asymmetry becomes negligible as Rayleigh number increases.

## Acknowledgment

We are grateful to Dr. Liliانا Mogni, Member of the Materials Characterization Group of the Bariloche Atomic Center, for the collaboration and support on the viscosity measurements. We also want to thank Professor Marcelo H. García from Ven Te Chow Hydrosystems Laboratory of the University of Illinois at Urbana-Champaign for the generous provision of hollow glass particles. And finally we are grateful to Laboratório Nacional de Computação Científica (LNCC) where some simulations were performed. We acknowledge financial support from Universidad Nacional de Cuyo (PBI 06/C457, 06/C423, 06/C428, C010) and Conicet (PIP 11420090100273).

## References

- [1] H. Buchberg, I. Catton, D.K. Edwards, Natural convection in enclosed spaces: a review of application to solar energy collection, *J. Heat Transf.* 98 (1976) 182–188.
- [2] J. Gastelurrutia, J.C. Ramos, G.S. Larraona, Numerical modelling of natural convection of oil inside distribution transformers, *Appl. Therm. Eng.* 31 (2011) 493–505.
- [3] G. De Vahl Davis, Natural convection of air in a square cavity: a benchmark numerical solution, *Int. J. Numer. Methods Fluids* 3 (1983) 249–264.
- [4] J.M. Hyun, J.W. Lee, Numerical solutions for transient natural convection in a square cavity with different sidewall temperatures, *Int. J. Heat Fluid Flow* 10 (1989) 146–151.
- [5] F. Arpino, N. Massarotti, A. Mauro, High Rayleigh number laminar-free convection in cavities: new benchmark solutions, *Numer. Heat Transf. Part B Fundam.* 58 (2010) 73–97.
- [6] P. Le Quére, Accurate solutions to the square thermally driven cavity at high Rayleigh number, *Comput. Fluids* 20 (1991) 29–41.
- [7] W. Hiller, S. Koch, T. Kowalewski, Three-dimensional structures in laminar natural convection in a cubic enclosure, *Exp. Therm. Fluid Sci.* 2 (1989) 34–44.
- [8] W. Leong, K. Hollands, A. Brunger, Experimental Nusselt numbers for a cubical-cavity benchmark problem in natural convection, *Int. J. Heat Mass Transf.* 42 (1998) 1979–1989.
- [9] W. Leong, K. Hollands, A. Brunger, On a physically-realizable benchmark problem in internal natural convection, *Int. J. Heat Mass Transf.* 41 (1998) 3817–3828.
- [10] M. Mamun, W. Leong, K. Hollands, D. Johnson, Cubical-cavity natural-convection benchmark experiments: an extension, *Int. J. Heat Mass Transf.* 46 (2003) 3655–3660.
- [11] G.D. Mallinson, G.D.V. Davis, Three-dimensional natural convection in a box: a numerical study, *J. Fluid Mech.* 83 (1977) 1–31.
- [12] B.A.V. Bennett, J. Hsueh, Natural convection in a cubic cavity: implicit numerical solution of two benchmark problems, *Numer. Heat Transf. Part A Appl.* 50 (2006) 99–123.
- [13] T. Fusegi, J. Hyun, K. Kuwahara, B. Farouk, A numerical study of three-dimensional natural convection in a differentially heated cubical enclosure, *Int. J. Heat Mass Transf.* 34 (1991) 1543–1557.
- [14] Y. Peng, C. Shu, Y.T. Chew, A 3d incompressible thermal lattice Boltzmann model and its application to simulate natural convection in a cubic cavity, *J. Comput. Phys.* 193 (2004) 260–274.
- [15] E. Tric, G. Labrosse, M. Betrouni, A first incursion into the 3d structure of natural convection of air in a differentially heated cubic cavity, from accurate numerical solutions, *Int. J. Heat Mass Transf.* 43 (2000) 4043–4056.
- [16] S. Wakashima, T.S. Saitoh, Benchmark solutions for natural convection in a cubic cavity using the high-order time-space method, *Int. J. Heat Mass Transf.* 47 (2004) 853–864.
- [17] D.W. Pepper, K.G.T. Hollands, Summary of benchmark numerical studies for 3-d natural convection in an air-filled enclosure, *Numer. Heat. Transf. A* 42 (2002) 1.
- [18] R. Janssen, R. Henkes, C. Hoogendoorn, Transition to time-periodicity of a natural-convection flow in a 3d differentially heated cavity, *Int. J. Heat Mass Transf.* 36 (1993) 2927–2940.
- [19] O. Younis, J. Pallares, F.X. Grau, Numerical study of transient laminar natural convection cooling of high Prandtl number fluids in a cubical cavity: influence of the Prandtl number, *Int. J. Appl. Sci. Eng. Technol.* 1 (2007) 107–112.
- [20] T. Yamasaki, F. Thomas, J. Irvine, Laminar free convection in a vertical tube with temperature-dependent viscosity, *Int. J. Heat Mass Transf.* 27 (1984) 1613–1621.
- [21] J.M. Hyun, J.W. Lee, Transient natural convection in a square cavity of a fluid with temperature-dependent viscosity, *Int. J. Heat Fluid Flow* 9 (1988) 278–285.
- [22] A. Emery, J. Lee, The effects of property variations on natural convection in a square enclosure, *J. Heat Transf.* 121 (1999) 57–62.
- [23] D.R. Chenoweth, S. Paolucci, Natural convection in an enclosed vertical air layer with large horizontal temperature differences, *J. Fluid Mech.* 169 (1986) 173–210.
- [24] S. Paolucci, D.R. Chenoweth, Transition to chaos in a differentially heated vertical cavity, *J. Fluid Mech.* 201 (1989) 379–410.
- [25] R. Codina, Comparison of some finite element methods for solving the diffusion-convection-reaction equation, *Comput. Methods Appl. Mech. Eng.* 156 (1998) 185–210.
- [26] R. Codina, A Finite Element Model for Incompressible Flow Problems, 1992. Ph.D. thesis.
- [27] A. Lew, El método de elementos finitos en entornos de alta performance, 1998. Master's thesis.
- [28] C. Perrier, A. Beroual, J. Bessede, Improvement of power transformers by using mixtures of mineral oil with synthetic esters, *Dielectr. Electr. Insul. IEEE Trans.* 13 (2006) 556–564.
- [29] V. Arpacı, A. Selamet, K. Shu-Hsin, Introduction Heat Transfer, Prentice Hall, 1999.
- [30] F. Incropera, D. DeWitt, Fundamentals of Heat and Mass Transfer, John Wiley and Sons, 1996.
- [31] R.J. Adrian, Particle-imaging techniques for experimental fluid mechanics, *Annu. Rev. Fluid Mech.* 23 (1991) 261–304.
- [32] M. Raffel, C. Willert, S. Wereley, J. Kompenhans, Particle Image Velocimetry: A Practical Guide, Springer-Verlag Berlin Heidelberg, 2007.
- [33] A. Schroder, C. Willert, Particle Image Velocimetry: New Developments and Recent Applications, vol. 112, Springer-Verlag Berlin Heidelberg, 2008.